



## Highly efficient CO<sub>2</sub> photoreduction by ultralow-Ru-Loading ZIF-67

Fangxu Dai <sup>a</sup>, Mingming Zhang <sup>a</sup>, Qian Chen <sup>a</sup>, Mingzhong Mi <sup>a</sup>, Zhenjiang Li <sup>b</sup>, Jishu Han <sup>a,\*</sup>, Jun Xing <sup>a,\*</sup>, Shouhua Feng <sup>a</sup>, Lei Wang <sup>a,c, \*\*</sup>

<sup>a</sup> Key Laboratory of Eco-chemical Engineering, Ministry of Education, College of Chemistry and Molecular Engineering, Qingdao University of Science and Technology, Qingdao 266042, PR China

<sup>b</sup> College of Materials Science and Engineering, Qingdao University of Science and Technology, Qingdao 266042, PR China

<sup>c</sup> College of Environment and Safety Engineering, Qingdao University of Science and Technology, Shandong Engineering Research Center for Marine Environment Corrosion and Safety Protection, Qingdao 266042, PR China



### ARTICLE INFO

**Keywords:**  
Ultra-low loading  
Co-catalyst  
Intermediate link  
Photocatalytic  
CO<sub>2</sub> reduction

### ABSTRACT

Developing highly efficient and low-cost photocatalysts for CO<sub>2</sub> reduction is of critical importance for the conversion of CO<sub>2</sub> to value-added chemicals. Here we report a Co-based zeolitic imidazole framework (ZIF-67) based photocatalyst with exceptional photocatalytic activity and durability for CO<sub>2</sub> reduction. ZIF-67 is doped with dicyandiamide (DCD), the intermediate link with the trace Ru cocatalyst (0.0127 wt. %). The underlying reduction mechanism was unraveled by the joint experiment-theory study. The strong orbital coupling of ZIF-67-DCD-Ru series structure leads to strong CO<sub>2</sub> adsorption, electron enrichment on cocatalyst, and minimum Gibbs free energy barrier of CO generation. The synthesized ZIF-67/DCD/Ru sample exhibits excellent CO<sub>2</sub> photoreduction performance with a CO generation rate of 1495 mmol g<sub>Ru</sub><sup>-1</sup> h<sup>-1</sup> and achieves a record turnover frequency (TOF) of 151 h<sup>-1</sup>, representing top-level photocatalytic activity among all reported ZIFs-based photocatalysts. For the first time, our work points out a novel way to achieve high activity of ultralow noble metal loading photocatalyst and provides an in-depth understanding of the advances of the series structure.

### 1. Introduction

Photocatalytic reduction of CO<sub>2</sub> to chemical feedstocks using solar energy is a promising pathway to solve energy depletion and environmental crisis [1–4]. Photoreduction of CO<sub>2</sub> with H<sub>2</sub>O to carbon monoxide (CO) or hydrocarbons is unfavorable in thermodynamics, because of the chemically inert nature of CO<sub>2</sub> and the high activation energy of the reaction [5–7]. So far, semiconductor-based photocatalysts such as oxides, chalcogenides, nitrides, phosphides, and metal-organic complexes have been developed to enhance the CO<sub>2</sub> adsorption, reduce the reaction barrier and improve the energy conversion efficiency [8–12]. Especially, zeolitic imidazole frameworks (ZIFs), as a subclass of metal-organic frameworks (MOFs), are emerging candidates for CO<sub>2</sub> photoreduction due to their controllable composition, porous structure, excellent chemical and thermal stability, as well as high CO<sub>2</sub> affinity [13–15]. Although ZIFs have fast charge transfer, they often suffer from limited redox capacity because of coordination saturated metal nodes

and few exposed active sites [16,17]. In general, a noble metal cocatalyst supported on a semiconductor is the most classical strategy promoting CO<sub>2</sub> photoreduction kinetically, which can trap photo-induced charges, accelerate electron-hole separation and facilitate the catalytic reaction effectively by reducing the potential barrier of the CO<sub>2</sub> conversion reaction [18–22]. However, the low abundance and high cost of the noble metals significantly limits their extensive application in catalytic materials. Therefore, it is desirable to achieve high activity targets with ultralow noble metal loadings [19,23].

Herein, we integrate the Co-based zeolitic imidazole framework (ZIF-67) with noble metal Ru cocatalyst by using dicyandiamide (DCD) as an intermediate linker to fabricate a composite photocatalyst for high-performance CO<sub>2</sub> reduction. In the sample ZIF-67/DCD/Ru, DCD small molecule additive with amine group can enhance CO<sub>2</sub> affinity. The series structure ZIF-67-DCD-Ru significantly enhances the CO<sub>2</sub> adsorption, facilitates charge separation and transfer, and reduced the energy barrier of CO<sub>2</sub> reduction. More importantly, under the ultra-low loading of

\* Corresponding authors.

\*\* Corresponding author at: Key Laboratory of Eco-chemical Engineering, Ministry of Education, College of Chemistry and Molecular Engineering, Qingdao University of Science and Technology, Qingdao 266042, PR China.

E-mail addresses: [jishu\\_han@163.com](mailto:jishu_han@163.com) (J. Han), [xingjun@qust.edu.cn](mailto:xingjun@qust.edu.cn) (J. Xing), [inorchemwl@126.com](mailto:inorchemwl@126.com) (L. Wang).

Ru (0.0127 wt. %), the composite ZIF-67/DCD/Ru exhibited excellent photocatalytic  $\text{CO}_2$  reduction to CO activity ( $189.86 \mu\text{mol g}^{-1}\text{catalyst h}^{-1}$ ), which is 12.2 times higher than for the pristine ZIF-67. The ZIF-based photocatalyst achieves a record turnover frequency (TOF) of  $151 \text{ h}^{-1}$ , far exceeding reported ZIF-based photocatalysts.

## 2. Methods and experimental section

### 2.1. Chemicals

Cobalt nitrate hexahydrate ( $\text{Co}(\text{NO}_3)_2 \cdot 6\text{H}_2\text{O}$ ), 2-methylimidazole, Hexadecyl trimethyl ammonium bromide (CTAB), Cyanamide (CA), Dicyandiamide (DCD), Tris(2,2'-bipyridine) dichlororuthenium(II) hexahydrate ( $[\text{Ru}(\text{bpy})_3]\text{Cl}_2 \cdot 6\text{H}_2\text{O}$ ) and Ruthenium(III) chloride anhydrous ( $\text{RuCl}_3$ ) were purchased from Aladdin Co. Ltd. (Shanghai, China) and used as received.

### 2.2. Synthesis of ZIF-67/DCD/Ru

ZIF-67/DCD/Ru was synthesized by a one-pot hydrothermal method. First, 290 mg  $\text{Co}(\text{NO}_3)_2 \cdot 6\text{H}_2\text{O}$  and 5 mg CTAB were dissolved in 10 mL deionized water (solution A), and 4.54 g 2-methylimidazole was dissolved in 70 mL deionized water (solution B). Then, solution A was rapidly injected into solution B with continuous stirring at room temperature. A purple precipitate formed immediately. Then, 1 g of DCD and 10 mg of  $[\text{Ru}(\text{bpy})_3]\text{Cl}_2 \cdot 6\text{H}_2\text{O}$  were sequentially added to the mixed solution. The mixed solution was heated in a Teflon-lined stainless steel autoclave (temperature programmed: the temperature was increased from room temperature to  $80^\circ\text{C}$  within 1 h, then held at  $80^\circ\text{C}$  for 6 h, then raised to  $120^\circ\text{C}$  within 1 h and kept for 15 h. The sample was

naturally cooled to room temperature). The obtained samples were washed three times with deionized water, dried at  $60^\circ\text{C}$  for 12 h and labeled as ZIF-67/DCD/Ru. The ZIF-67/CA/Ru sample was prepared using the same procedure, replacing the corresponding DCD with CA (1 g). ZIF-67/DCD (CA) and ZIF-67/Ru samples were synthesized with the same procedure as mentioned above without adding  $[\text{Ru}(\text{bpy})_3]\text{Cl}_2 \cdot 6\text{H}_2\text{O}$  or DCD (CA) respectively.

## 3. Results and discussion

### 3.1. Synthesis and structural characterization of photocatalysts

The sample ZIF-67/DCD/Ru was fabricated by a one-pot hydrothermal method. Control, ZIF-67/Ru and ZIF-67/DCD, were prepared by adding only  $[\text{Ru}(\text{bpy})_3]\text{Cl}_2 \cdot 6\text{H}_2\text{O}$  or DCD to the ZIF-67 precursor, respectively. Transmission electron microscopy (TEM) was performed to detect the morphology and microstructure of the ZIF-67 hybrids. The pristine ZIF-67 shows a cubic structure with a diameter of about 320 nm and rounded edges (Fig. S1a). For the samples ZIF-67/DCD/Ru, ZIF-67/Ru and ZIF-67/DCD, the cubic shape and size of the crystals are well maintained and no additional impurities are observed (Fig. 1a and S1b, c). Energy dispersive spectroscopy (EDS) elemental mapping demonstrates that C, N, and Co elements are well distributed throughout the ZIF-67/DCD/Ru (Fig. 1b). The amount of loaded Ru in sample ZIF-67/DCD/Ru was determined to be 0.0127 wt. % by inductively coupled plasma optical emission spectrometry (ICP-OES) (Table S1). However, the content of Ru in the sample ZIF-67/Ru is as low as 0.0003 wt. %. It can be concluded that the DCD molecules in the sample ZIF-67/DCD/Ru play the role of linker combining ZIF-67 and Ru. The Powder X-ray diffraction (PXRD) pattern of pristine ZIF-67 has diffraction peaks at

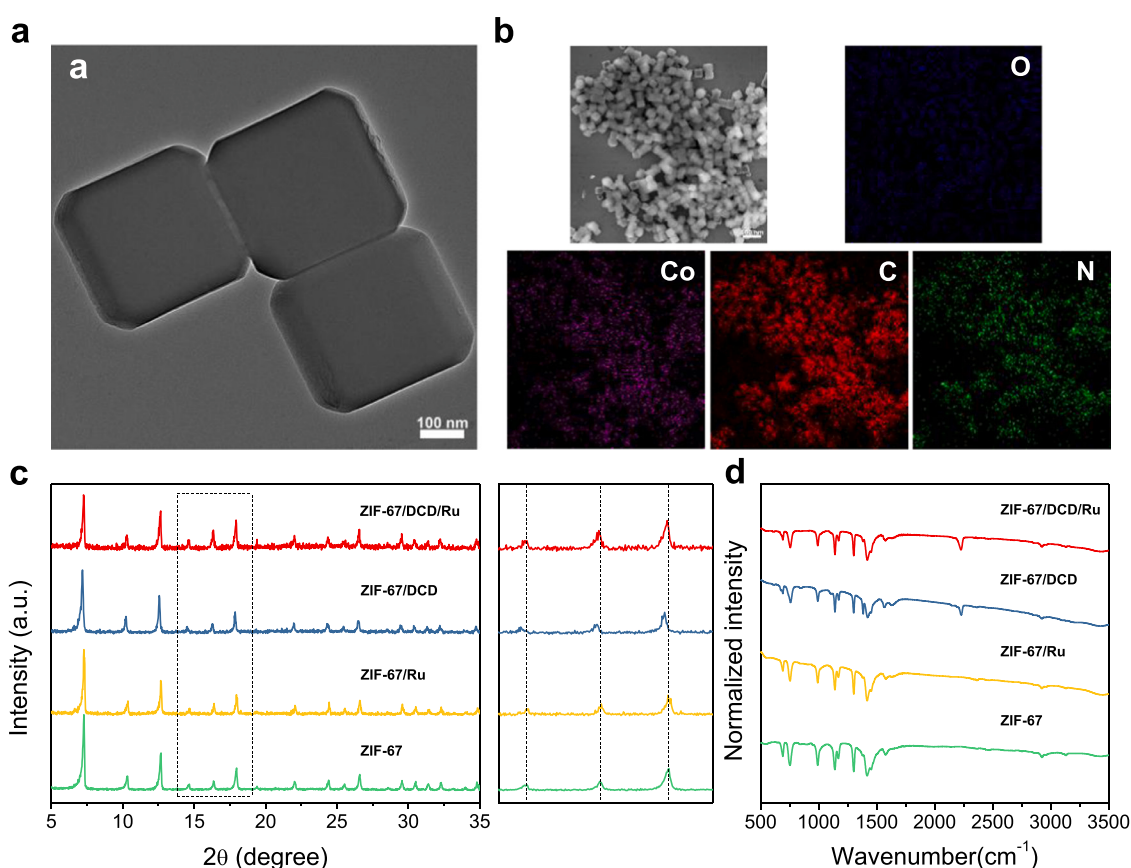


**Fig. 1.** (a) TEM images of ZIF-67/DCD/Ru. (b) EDS elemental mapping of ZIF-67/DCD/Ru shows the locations of O, Co, C, and N. (c) XRD patterns of ZIF-67, ZIF-67/Ru, ZIF-67/DCD, and ZIF-67/DCD/Ru. Local enlargement of the region of blue dashed rectangle in (c). (d) DRIFT spectra of ZIF-67, ZIF-67/Ru, ZIF-67/DCD, and ZIF-67/DCD/Ru.

around 7.4, 10.4, 12.7, 14.4, 16.5, and 18.1°, which can be indexed to the (001), (002), (112), (022), (013) and (222) lattice planes, respectively (Fig. 1c) [24]. The sample ZIF-67/Ru shows the same PXRD pattern as pristine ZIF-67. However, the PXRD peaks of ZIF-67/DCD and ZIF-67/DCD/Ru slight shift towards small angles compared to pristine ZIF-67, suggesting the DCD molecules dope into the pore structures of the ZIF-67 and result in lattice expansion of unit cell [21,25,26]. The N<sub>2</sub> adsorption-desorption isotherms measurements illustrate that the Brunauer-Emmett-Teller (BET) surface area of ZIF-67 is 1289.5 m<sup>2</sup>/g, however, the surface area of ZIF-67/DCD/Ru drops to 613.9 m<sup>2</sup>/g, which further confirm that DCD/Ru molecules fill in the pores of ZIF-67 (Fig. S2a,b) [14]. The C/N ratio of DCD molecule is much lower than that of ZIF-67, therefore the DCD/Ru dopant decreases the C/N ratio of ZIF-67/DCD/Ru (1.73) compared to pristine ZIF-67 (1.80) (Table S2) [27]. In Fig. 1d, the Fourier transform infrared (FT-IR) spectra of these samples have the vibrational peaks at 600–1500, 1580, 2927, and 3132 cm<sup>-1</sup>, which are mainly attributed to the ligand 2-methylimidazole. Meanwhile, for the DCD or DCD/Ru modified ZIF-67, new vibrational signal appearing at 2235 cm<sup>-1</sup> reflects the stretching vibration of the nitrile group (C≡N) [28].

X-ray photoelectron spectroscopy (XPS) reveals the elemental composition and surface chemical states of the samples ZIF-67, ZIF-67/Ru, ZIF-67/DCD, and ZIF-67/DCD/Ru. As shown in Fig. 2a, the three main peaks at 284.6, 285.9, and 288.5 eV for the C 1s XPS spectra are corresponding to the C=C, C-C, and N-C≡N, respectively [13,29]. The featured peak area of N-C≡N at 288.5 eV in DCD-modified ZIF-67 is weakened, which might be attributed to the coordination environment changes (Table S3). There are three nitrogen signals in the N 1s XPS spectra of at 398.5 eV, 399.0 eV, and 399.9 eV, which are assigned to pyridinic N, pyrrolic N and metal-N<sub>4</sub> (Fig. 2b) [31]. The main peak at 198.6 eV of the Cl 2p spectra is only observed in ZIF-67/DCD/Ru (Fig. 2c). The sample ZIF-67/Ru shows negligible signal in the Cl 2p spectrum due to the much low content of Ru. The Co 2p XPS spectra reveal double peaks at 781.3 and 797.1 eV, corresponding to Co 2p<sub>3/2</sub>

and 2p<sub>1/2</sub>, respectively, namely that the Co<sup>2+</sup> cations exist in the samples (Fig. S3a). There is no signal of Ru element in the sample of ZIF-67/DCD/Ru due to the ultra-low loading and distribution inside the pores of ZIF-67 (Fig. 2a and Fig. S3b) [30]. In addition, the CO<sub>2</sub> capture capacity of the composite materials was evaluated. As shown in Fig. 2d, the pristine ZIF-67 sample has a high CO<sub>2</sub> adsorption capacity of 31.5 cm<sup>3</sup> g<sup>-1</sup>, which would contribute to the heterogeneous CO<sub>2</sub> reduction reaction. In contrast, the CO<sub>2</sub> adsorption capacity of the obtained ZIF-67/DCD/Ru with lower specific surface area increases by 3.5 cm<sup>3</sup> g<sup>-1</sup>, due to enhanced CO<sub>2</sub> affinity, attributed to the amine molecule dopants [24,32].

### 3.2. Photo-responsive characterization of photocatalysts

Ultraviolet-visible (UV-Vis) diffuse reflectance spectroscopy measurements were performed to characterize the semiconductor-like behavior of the ZIF-67 based photocatalysts (Fig. 3a). The pristine ZIF-67 exhibits an absorption edge at 370 nm with spin-coupling triplet peaks at 585, 564, and 539 nm, corresponding to the spin-allowed energy transition of <sup>4</sup>A<sub>2</sub>(F)-<sup>4</sup>T<sub>1</sub>(P) d-d Co [24]. The absorption edge of ZIF-67/DCD/Ru exhibits a slight redshift because of weakened interaction of atoms induced by the crystal lattice expansion. The bandgap can be calculated by the formula:  $\Delta h\nu = A(\hbar\nu - E_g)^{n/2}$ . As shown in Fig. S4a, the bandgap of ZIF-67 was determined to be 1.99 eV. The positive slopes derived from the Mott-Schottky (MS) plots of material indicate that ZIF-67 is an n-type semiconductor, with the flat band potential (E<sub>fb</sub>) of ZIF-67 is -0.93 eV (vs. Ag/AgCl) (Fig. S4b) [31]. Therefore, the conduction band value of ZIF-67 is -0.69 eV vs. NHE, and the corresponding valence band value of ZIF-67 is 1.30 eV. The valence band value of ZIF-67 is more positive than the oxidation potential of O<sub>2</sub>/H<sub>2</sub>O (1.23 V vs. NHE), meanwhile its conduction band value is more negative than the reduction potential of CO<sub>2</sub>/CO (-0.12 V vs. NHE) and CO<sub>2</sub>/CH<sub>4</sub> (-0.24 V vs. NHE). Photoluminescence (PL) and time-resolved PL (TRPL) measurements were performed to reveal the separation and

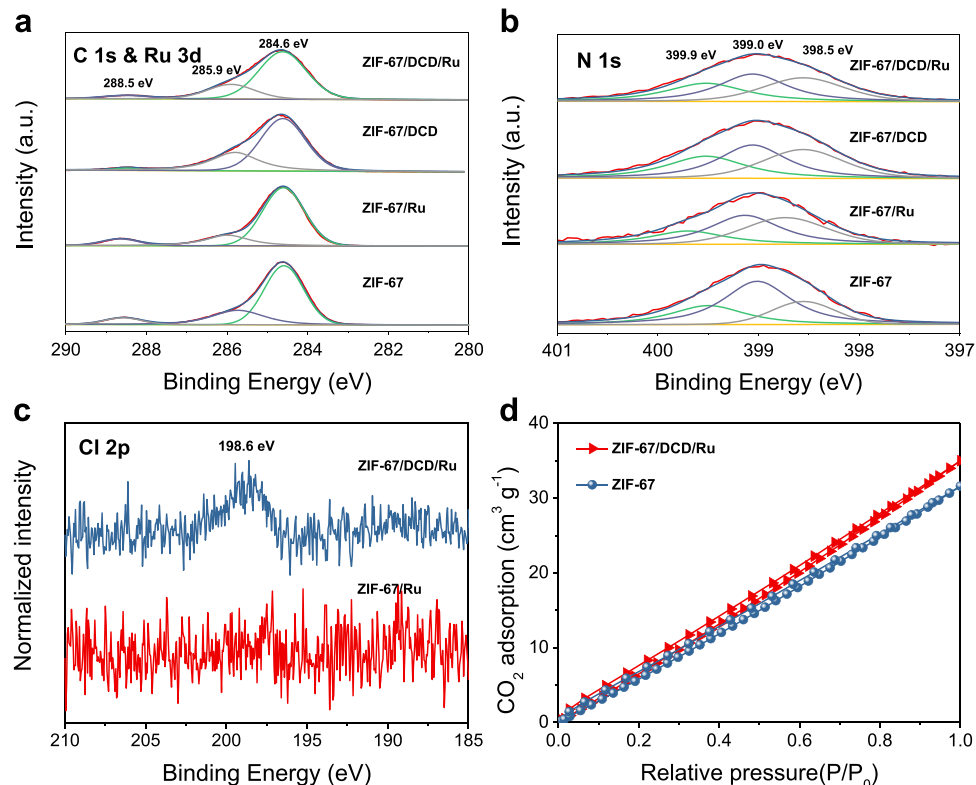
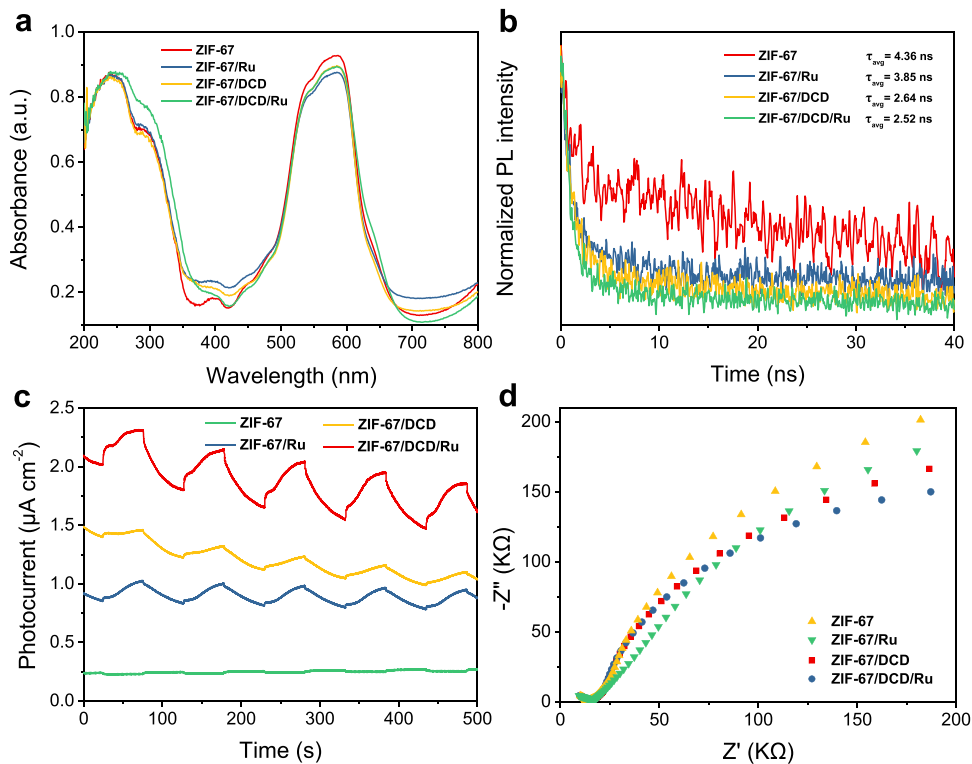


Fig. 2. (a) C 1s & Ru 3d, (b) N 1s, (c) Cl 2p XPS spectra of ZIF-67, ZIF-67/Ru, ZIF-67/DCD, and ZIF-67/DCD/Ru samples. (d) Comparisons in CO<sub>2</sub> adsorption of ZIF-67 and ZIF-67/DCD/Ru at 273 K.



**Fig. 3.** (a) UV-vis adsorption spectra, (b) TRPL spectra, (c) photocurrent response, and (d) electrochemical impedance spectra of ZIF-67, ZIF-67/Ru, ZIF-67/DCD, and ZIF-67/DCD/Ru samples.

transfer of photo-induced charge carriers. As shown in Fig. S5, the pure ZIF-67 exhibits a strong PL intensity at 467 nm, ZIF-67/Ru and ZIF-67/DCD show relatively weak PL intensity, ZIF-67/DCD/Ru display the lowest PL intensity. The PL decay times of these samples have the same order as their PL intensities. The  $\tau_{avg}$  for ZIF-67, ZIF-67/Ru, ZIF-67/DCD, and ZIF-67/DCD/Ru are 4.36, 3.85, 2.64, and 2.52 ns,

respectively (Fig. 3b). The decreased recombination of charge carriers in ZIF-67/DCD/Ru can be attributed to the efficient separation and transfer of photo-induced charge carriers from the semiconductor ZIF-67 to the electron trap DCD/Ru. The photocurrent density was measured to evaluate the transient photocurrent response under Xe lamp illumination. As shown in Fig. 3c, pristine ZIF-67 shows relatively poor

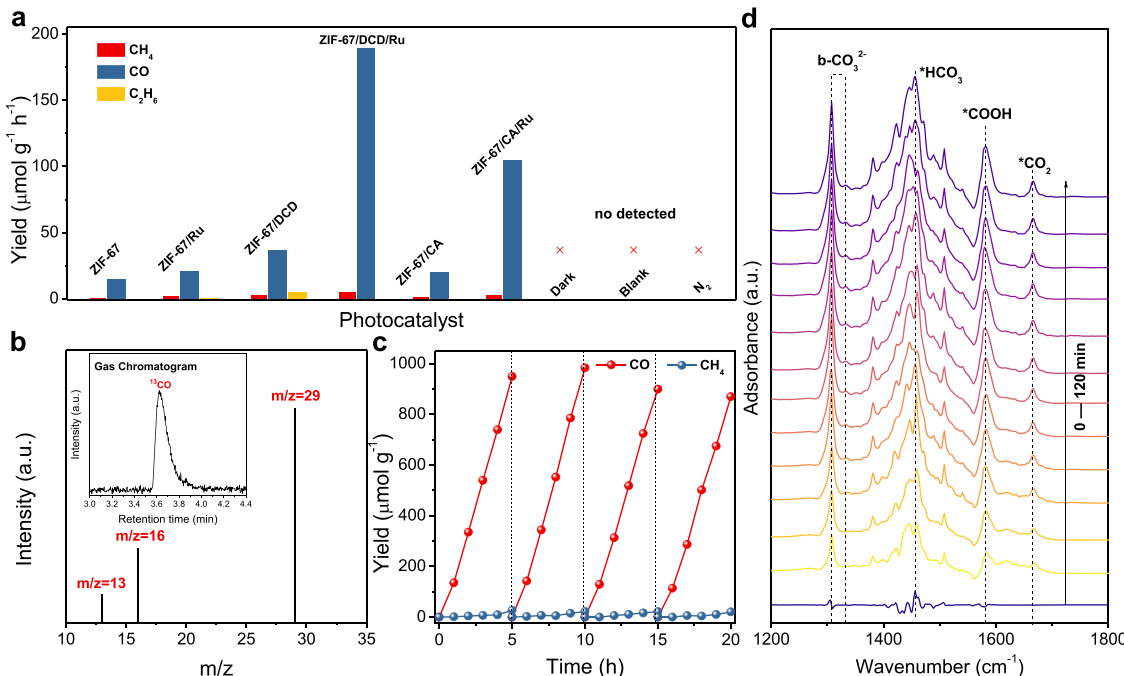


**Fig. 4.** (a) Photocatalytic  $\text{CO}_2$  reduction activity of ZIF-67, ZIF-67/Ru, ZIF-67/DCD, ZIF-67/DCD/Ru, ZIF-67/CA, and ZIF-67/CA/Ru. (b) GC-MS analysis of  $^{13}\text{CO}$  ( $m/z = 29$ ) products for photocatalytic  $^{13}\text{CO}_2$  reduction over ZIF-67/DCD/Ru. (c) The photoreduction cycling of  $\text{CO}_2$  of ZIF-67/DCD/Ru. (d) In situ FTIR spectra taken on ZIF67/DCD/Ru during  $\text{CO}_2$  photoreduction reaction.

photocurrent response. The sample ZIF-67/DCD/Ru has the highest photocurrent density than that of ZIF-67/DCD and ZIF-67/Ru, meaning better light response and more efficient photoinduced electron–hole separation [10,33]. Electrochemical impedance spectroscopy (EIS) measurements were performed to investigate the interfacial charge transfer between electrodes/electrolytes, where the semicircle in the Nyquist plots exhibits the charge transfer process, and the radius is inversely proportional to the charge transfer resistance [34]. As expected, ZIF-67/DCD/Ru shows the smallest radius compared to ZIF-67, ZIF-67/Ru, and ZIF-67/DCD (Fig. 3d). Fig. S6 shows the Mott–Schottky curves with slopes of 6.5 and 1.8 for ZIF-67 and ZIF-67/DCD/Ru. According to the formula:  $N_d = \frac{2}{\epsilon_0 \epsilon_0 \epsilon_r} (dc^{-2}/dV)^{-1}$ , it can be calculated that the electronic density of ZIF-67/DCD/Ru is 3.6 times that of ZIF-67 [35]. High electron density can promote exciton dissociation and charge carrier diffusion. Above results illustrate that the DCD/Ru modified ZIF-67 can effectively enhance the electron–hole separation, thereby promote the photocatalytic activity.

### 3.3. $\text{CO}_2$ photoreduction study

The photocatalytic  $\text{CO}_2$  reduction performance was evaluated by solid-vapor reaction mode in  $\text{CO}_2$  and steam atmosphere. As shown in Fig. 4a, pristine ZIF-67 shows poor photocatalytic  $\text{CO}_2$  reduction activity, the CO and  $\text{CH}_4$  yields are 15.61 and 0.36  $\mu\text{mol g}^{-1} \text{h}^{-1}$ . For the ZIF-67/Ru sample, the CO and  $\text{CH}_4$  yields increase slightly, reaching 21.18 and 1.08  $\mu\text{mol g}^{-1} \text{h}^{-1}$ , while trace amounts of  $\text{C}_2\text{H}_6$  (0.33  $\mu\text{mol g}^{-1} \text{h}^{-1}$ ) was produced. Compared with ZIF-67, the CO yield of ZIF-67/DCD was significantly improved; the yields of CO,  $\text{CH}_4$ , and  $\text{C}_2\text{H}_6$  are 36.94, 1.93, and 4.84  $\mu\text{mol g}^{-1} \text{h}^{-1}$ , respectively. The DCD additive can promote the interfacial electron transfer of the photocatalyst and improve  $\text{CO}_2$  adsorption ability. In recent years, more and more studies have been carried out on ZIF-based composites, such as  $\text{TiO}_2/\text{C@ZnCo-ZIF-L}$ ,  $\text{ZnAl-LDH@ZIF-8}$ ,  $\text{CsPbBr}_3@\text{ZIF-67(1,4)}$ ,  $\text{CdS/ZIF-8}$ , etc, which exhibit higher performance than that of pristine ZIF materials. Noble metal cocatalysts are normally introduced to improve the photocatalytic activity of the composites, however, these reported photocatalysts still suffer from low TOF due to the low utilization rate and catalytic activity of their cocatalysts. Remarkably, the CO and  $\text{CH}_4$  generation rates of ZIF-67/DCD/Ru are as high as 189.86 and 4.15  $\mu\text{mol g}^{-1} \text{h}^{-1}$ , which is 12.2 times that of pristine ZIF-67. Its CO selectivity reaches 97.86 % (Fig. S7). The photocatalytic activity and corresponding TOF of  $\text{CO}_2$  reduction, calculated based on Ru cocatalyst on the photocatalyst, is 1495  $\text{mmol g}_{\text{Ru}}^{-1} \text{h}^{-1}$  and 151  $\text{h}^{-1}$ , which are the highest activities over all reported ZIF-based photocatalysts (Table S4,5). No  $\text{H}_2$  was detected during the photocatalytic reaction, indicating that  $\text{CO}_2$  reduction is prior to  $\text{H}_2\text{O}$  reduction. Fig. S8 shows the temporal profiles of the  $\text{CO}_2$  photoreduction on different photocatalysts. The linear increase of CO product with irradiation time suggests the progress of the photocatalytic reaction (Fig. S8a). As shown in Fig. S8b, the oxidation product  $\text{O}_2$  was detected due to the photogenerated holes reacting with  $\text{H}_2\text{O}$  molecules. The yield of  $\text{O}_2$  is approximately proportional to the yield of CO. When the amount of Ru or DCD increases/decreases, the CO yield would decline (Fig. S9a,b). Appropriate amount was important to achieve the optimal CO production rates for ZIF-67/DCD/Ru photocatalysts. The ZIF-67/DCD/Eosin Y sample exhibits 42.5  $\mu\text{mol g}^{-1} \text{h}^{-1}$  CO yields, which is as low as ZIF-67/DCD (Fig. S9c). Photocatalytic  $\text{CO}_2$  reduction was further confirmed by a series of control experiments under different conditions 1) dark reaction, 2) without photocatalyst, and 3)  $\text{N}_2$  atmosphere, with no detectable product (Fig. 4a). As shown in Fig. 4b, the isotope labeling experiment with  $^{13}\text{CO}_2$  as the substrate was carried out to confirm the origin of CO. The GC analysis shows a peak with a retention time of 3.63 min, which corresponds to CO. While a  $^{13}\text{CO}$  ( $m/z = 29$ ) signal was detected in MS. The GC-MS results confirm that CO is the product of the photocatalytic reduction of  $\text{CO}_2$ . The cycling performance of the ZIF-67/DCD/Ru photocatalyst was monitored to detect the

durability of the photocatalyst (Fig. 4c). The continuous yield of CO and  $\text{CH}_4$  for up to 20 h under light irradiation, implies good photochemical stability of the catalyst. As shown in Fig. S10, the stability of ZIF-67/DCD/Ru was detected by XRD and TEM measurement. After the photocatalytic  $\text{CO}_2$  reduction test for 20 h, ZIF-67/DCD/Ru maintains its structure and morphology, suggesting the fine stability of the ZIF-based photocatalyst.

To extend the feasibility of this strategy, we also synthesized ZIF-67/CA (cyanamide) and ZIF-67/CA/Ru photocatalysts. As expected, the photocatalyst ZIF-67/CA/Ru also shows enhanced photocatalytic performance, of which the CO and  $\text{CH}_4$  yields are as high as 105.01 and 2.11  $\mu\text{mol g}^{-1} \text{h}^{-1}$  (Fig. 4a). Its CO selectivity even reaches 98.03 % (Fig. S7). We further characterized these photocatalysts to study the influence of CA/Ru modification on ZIF-67. Interestingly, compared with DCD/Ru addition, the morphology of the ZIF-67 crystals transform from cubic to rhombic nanocrystal after CA/Ru modification, of which the diameter increases to about 650 nm (Fig. S11). The weight ratio of Ru was measured to be 0.0012 wt. %. Compared with the pristine ZIF-67, the XRD peaks of CA modified samples also shows slight shift towards small angle and low C/N ratio (1.67) (Fig. S12 and Table S2).

To clarify the  $\text{CO}_2$  photoreduction reaction pathway, we conducted *in-situ* diffuse reflectance infrared Fourier transform spectra (DRIFTS) measurements on ZIF-67/DCD/Ru. As shown in Fig. 4d, the peaks at 1308, 1330 and 1581  $\text{cm}^{-1}$  can be assigned to the b- $\text{CO}_3^{2-}$  and C=O stretch of  $^{*}\text{COOH}$ , respectively, which are considered to be vital intermediates in the formation and conversion of  $^{*}\text{CO}$  to CO [20,34]. The band at 1455  $\text{cm}^{-1}$  can be assigned to the symmetric stretching of  $^{*}\text{HCO}_3$ . The signal of  $^{*}\text{CO}_2$  (1667  $\text{cm}^{-1}$ ) is much weaker than that of  $^{*}\text{COOH}$ , indicating that the fast transformation process of  $^{*}\text{CO}_2$  to  $^{*}\text{COOH}$ . In the sample ZIF-67/DCD/Ru, DCD additive with amine group can enhance  $\text{CO}_2$  affinity. The amine group with great polarity would bond with the  $\text{CO}_2$  molecule by hydrogen bonding. According to previous studies, the interaction of the amino group and  $\text{CO}_2$  will bend the linear bond of O=C=O slightly, promoting the activation of  $\text{CO}_2$  to form  $^{*}\text{COOH}$  intermediates [36–38]. According to the  $\text{CO}_2$  reaction pathway,  $\text{CO}_2$  molecule is activated at the neighboring Ru site, and then reacts with electrons and protons to generate the intermediate  $^{*}\text{COOH}$ , which can be subsequently split into  $^{*}\text{CO}$  and produce CO after desorption.

### 3.4. DFT study

Density functional theory (DFT) calculations were carried out to gain insight into the  $\text{CO}_2$  photoreduction activity and selectivity of ZIF-67/DCD/Ru at the atomic level. Based on the afore mentioned studies, we constructed four models ZIF-67, ZIF-67/Ru, ZIF-67/DCD, and ZIF-67/DCD/Ru (Fig. S13). These models are based on the stable structure of ZIF-67 and represent the likely coordination geometries of DCD, Ru, and DCD/Ru to ZIF-67. In general, the photocatalytic  $\text{CO}_2$  reduction reaction undergoes the pathways in the order of  $\text{CO}_2$ ,  $^{*}\text{CO}_2$ ,  $^{*}\text{COOH}$ ,  $^{*}\text{CO}$ ,  $^{*}\text{CHO}$ ,  $^{*}\text{CH}_2\text{O}$ ,  $^{*}\text{CH}_3\text{O}$ ,  $^{*}\text{CH}_3\text{OH}$ ,  $^{*}\text{CH}_3$ , and  $^{*}\text{CH}_4$  [39]. The formation of  $^{*}\text{COOH}$  intermediates is generally regarded as the rate-determining step for  $\text{CO}_2$ -to-CO due to the electron-coupled proton transfer reaction with high energy barrier (Fig. S14–17). As shown in Fig. 5a, the Gibbs free energy ( $\Delta G$ ) diagram of the  $\text{CO}_2$  reduction process illustrates the  $\Delta G$  of the first electron-coupled proton transfer step ( $^{*}\text{CO}_2 + \text{H}^+ + \text{e}^- \rightarrow ^{*}\text{COOH}$ ) on pure ZIF-67 is 0.87 eV. The  $\text{CO}_2$  molecules can hardly be activated on the Co center of ZIF-67. The Ru or DCD modified ZIF-67 has relatively low energy barrier in this step, which are 0.65 and 0.52 eV, respectively. When  $\text{CO}_2$  adsorbs on Co-DCD-Ru site in ZIF-67/DCD/Ru, the  $\Delta G$  of  $^{*}\text{COOH}$  formation significantly goes down to 0.40 eV, which contributes to the high  $\text{CO}_2$  photoreduction activity. The Gibbs free energy calculation results are consistent with DRIFTS measurements. Subsequent conversion of  $^{*}\text{COOH}$  to  $^{*}\text{CO}$  ( $^{*}\text{COOH} + \text{H}^+ + \text{e}^- \rightarrow ^{*}\text{CO} + \text{H}_2\text{O}$ ) is exothermic process and expected to occur spontaneously [32]. Finally, the  $^{*}\text{CO}$  intermediates will desorb from the ZIF-67 surface to

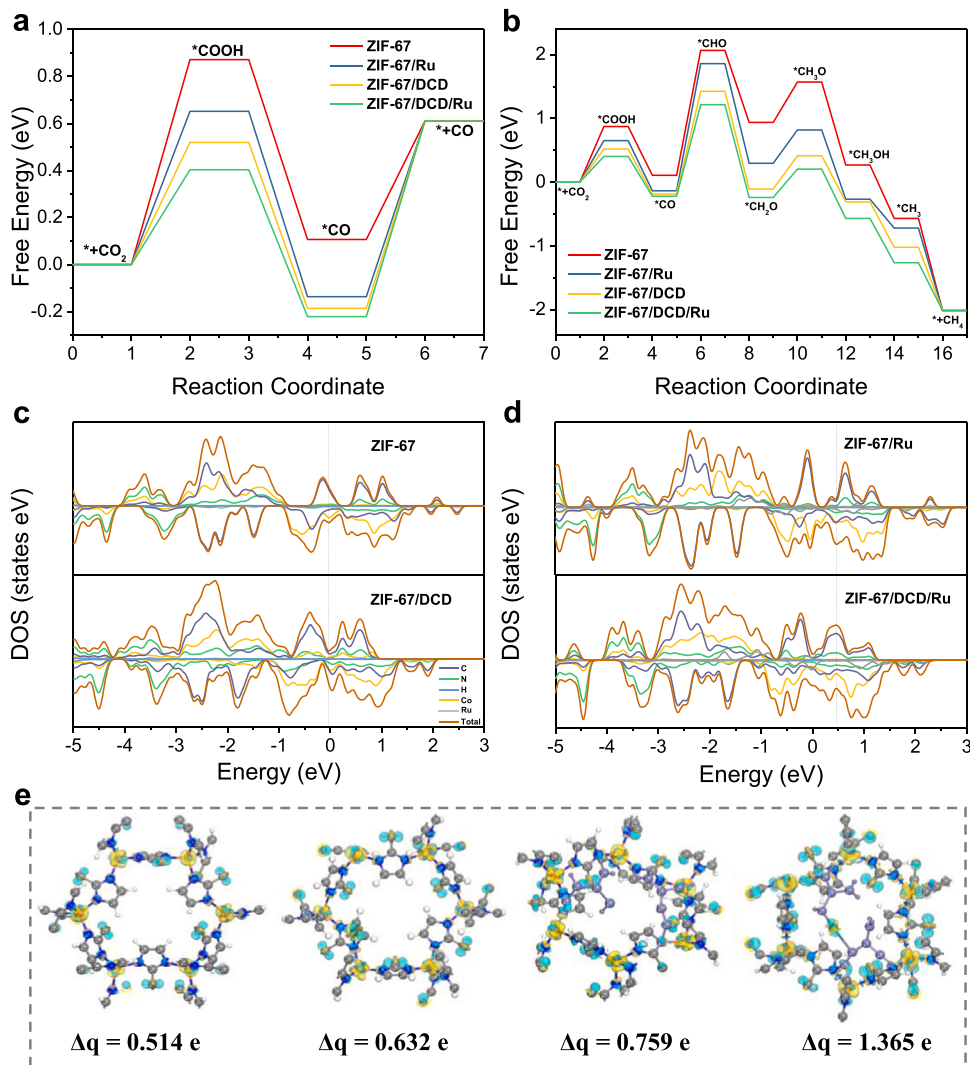


**Fig. 5.** (a, b) Gibbs free energy diagram of  $\text{CO}_2$  reduction pathway of ZIF-67, ZIF-67/Ru, ZIF-67/DCD, and ZIF-67/DCD/Ru samples. Calculated DOS of (c) ZIF-67 and ZIF-67/DCD, (d) ZIF-67/Ru and ZIF-67/DCD/Ru. (e) Charge density of ZIF-67, ZIF-67/Ru, ZIF-67/DCD, and ZIF-67/DCD/Ru samples.

form CO molecules (ZIF-67, ZIF-67/Ru, ZIF-67/DCD, and ZIF-67/DCD/Ru have energy barrier of 0.50, 0.75, 0.79, and 0.83 eV, respectively), while a part of  $^*\text{CO}$  intermediates will continue to be activated to transform towards the high-value product  $\text{CH}_4$ . Overall, the energy barriers of the  $\text{CH}_4$  generation on the four models are much higher than that of the CO generation path (Fig. 5b). Therefore, we got the high selectivity of  $\text{CO}_2$  photoreduction to CO.

The density of states (DOS) of ZIF-67, ZIF-67/Ru, ZIF-67/DCD, and ZIF-67/DCD/Ru were also implemented to elucidate their electronic structures (Fig. 5c,d). The strong orbital coupling of C, N, H, Co, and Ru atoms leads to strong adsorption, which confirms that the series structure of Co-DCD-Ru is beneficial to the electrons enrichment on ZIF-67/DCD/Ru, creating conditions for the  $\text{CO}_2$  reduction process. The d-band center of the adsorption sites in the four model photocatalysts depends on its local coordination environment, the value of ZIF-67, ZIF-67/Ru, ZIF-67/DCD and ZIF-67/DCD/Ru increase gradually from  $-1.792$  to  $-1.206$ ,  $-0.906$  and  $-0.715$  eV (Fig. S18a-d) [34]. This d-band center of the average adsorption site is precisely related to the adsorption energy of the  $^*\text{COOH}$  intermediate, and the closer d-band center to the Fermi level would induce the higher catalytic activity of  $^*\text{COOH}$  formation. In the end, the charge redistribution around the ZIF-67-DCD-Ru interface was investigated. As shown in Fig. 5e, we performed differential charge density diagrams with electron accumulation (yellow) and depletion (cyan) at the catalyst interface. In order to understand the

interaction between DCD, Ru, and DCD/Ru, Bader charge analysis were carried out for four catalytic models. Compared with ZIF-67 (0.514 e), ZIF-67/Ru (0.632 e), and ZIF-67/DCD (0.759 e), ZIF-67/DCD/Ru (1.365 e) will loses more electrons, which indicates that DCD/Ru can effectively promote the electron transfer of ZIF-67/DCD/Ru. Accordingly, the enhanced electron interaction endowed ZIF-67/DCD/Ru more favorable to activate  $\text{CO}_2$  reduction. As shown in Fig. 6, we proposed the catalytic reaction mechanism. The photocatalytic  $\text{CO}_2$  reduction reaction includes several steps: (1) photoexcitation to generate electron-hole pairs in ZIF-67; (2) electrons transfer from the conduction band of ZIF-67 to DCD-Ru; (3) electrons are trapped by the catalytic site of DCD-Ru, and react with adsorbed  $\text{CO}_2$  on the Ru site. The  $\text{CO}_2$  molecule is activated on the Ru site, then reacts with electrons and protons to generate the intermediate  $^*\text{COOH}$ , which subsequently split into  $^*\text{CO}$  and produces CO after desorption. Meanwhile, photogenerated holes react with  $\text{H}_2\text{O}$  to produce  $\text{O}_2$  on Co site in ZIF-67.

#### 4. Conclusions

In summary, ZIF-67 based photocatalysts were prepared by a one-pot hydrothermal method. A intermediate DCD dopant links the ZIF-67 and trace amounts of classical cocatalyst Ru to form series structure ZIF-67-DCD-Ru, which significantly enhances the photocatalytic  $\text{CO}_2$  reduction activity of the parent ZIF-67. Experimental analysis and DFT

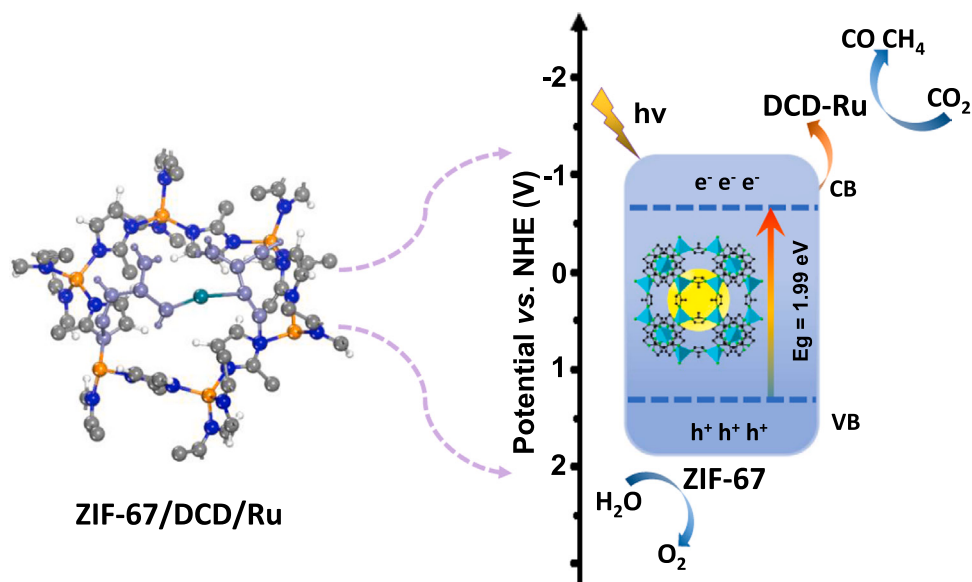


**Fig. 6.** Schematic diagram of photocatalytic  $\text{CO}_2$  reduction on ZIF-67/DCD/Ru.

calculations show that the strong orbital coupling of ZIF-67, DCD and Ru leads to strong  $\text{CO}_2$  adsorption, electron enrichment on the cocatalyst, and minimum Gibbs free energy barrier of CO generation. As a result, the sample ZIF-67/DCD/Ru can reduce  $\text{CO}_2$  to CO and  $\text{CH}_4$  with high selectivity of 97.86 %, excellent CO yield of  $1495 \text{ mmol g}_{\text{Ru}}^{-1} \text{ h}^{-1}$  and record TOF of over  $151 \text{ h}^{-1}$ . This study provides insights into the rational design of coordination catalysts for efficient  $\text{CO}_2$  photoreduction.

#### CRediT authorship contribution statement

**Jun Xing, Lei Wang and Shouhua Feng:** Conceived the idea and supervised the project. **Fangxu Dai:** Designed the experiments, prepared the samples, performed the sample characterizations, photocatalysis measurements, and wrote the manuscript. **Jishu Han, Zhenjiang Li and Mingzhong Mi:** First-principle calculations and analyzed the theoretical results. **Mingming Zhang and Qian Chen:** Performed the optical measurements. All authors read and commented on the manuscript.

#### Declaration of Competing Interest

The authors declare that they have no known competing financial interests or personal relationships that could have appeared to influence the work reported in this paper.

#### Data Availability

No data was used for the research described in the article.

#### Acknowledgments

This work was supported by the National Natural Science Foundation of China (51802171, 52072197), Outstanding Youth Foundation of Shandong Province, China (ZR2019JQ14), Youth Innovation and Technology Foundation of Shandong Higher Education Institutions, China (2019KJC004), Major Scientific and Technological Innovation Project (2019JZZY020405), Taishan Scholar Program, Major Basic Research Program of Natural Science Foundation of Shandong Province under Grant (ZR2020ZD09).

#### Appendix A. Supporting information

Supplementary data associated with this article can be found in the online version at [doi:10.1016/j.apcatb.2023.122934](https://doi.org/10.1016/j.apcatb.2023.122934).

#### References

- [1] G. Pacchioni, H. Freund, Controlling the charge state of supported nanoparticles in catalysis: lessons from model systems, *Chem. Soc. Rev.* 47 (2018) 8474–8502, <https://doi.org/10.1039/C8CS00152A>.
- [2] X. Li, J. Yu, M. Jaroniec, X. Chen, Cocatalysts for selective photoreduction of  $\text{CO}_2$  into solar fuels, *Chem. Rev.* 119 (2019) 3962–4179, <https://doi.org/10.1021/acs.chemrev.8b00400>.
- [3] W. Gao, S. Liang, R. Wang, Q. Jiang, Y. Zhang, Q. Zheng, B. Xie, C. Toe, X. Zhu, J. Wang, L. Huang, Y. Gao, Z. Wang, C. Jo, Q. Wang, L. Wang, Y. Liu, A. Roger, R. Amal, B. Louis, J. Scott, H. He, S. Parket, Industrial carbon dioxide capture and utilization: state of the art and future challenges, *Chem. Soc. Rev.* 49 (2020) 8584–8686, <https://doi.org/10.1039/D0CS00025F>.
- [4] T. Tan, B. Xie, Y. Ng, S. Abdullah, H. Tang, N. Bedford, R. Taylor, K. Zinsou, R. Amal, J. Scott, Unlocking the potential of the formate pathway in the photo-assisted Sabatier reaction, *Nat. Catal.* 3 (2020) 1034–1043, <https://doi.org/10.1038/s41929-020-00544-3>.
- [5] J. Kim, D. Hong, J. Lee, H. Kim, S. Lee, S. Shin, B. Kim, H. Lee, M. Kim, J. Oh, G. Lee, D. Nam, Y. Joo, Quasi-graphitic carbon shell-induced Cu confinement promotes electrocatalytic  $\text{CO}_2$  reduction toward  $\text{C}_{2+}$  products, *Nat. Commun.* 12 (2021) 3765–3775, <https://doi.org/10.1038/s41467-021-24105-9>.
- [6] C. Gao, S. Chen, Y. Wang, J. Wang, X. Zheng, J. Zhu, L. Song, W. Zhang, Y. Xiong, Heterogeneous single-atom catalyst for visible-light-driven high-turnover  $\text{CO}_2$  reduction: the role of electron transfer, *Adv. Mater.* 30 (2018) 1704624–1704632, <https://doi.org/10.1002/adma.202001848>.
- [7] Y. Pan, Y. Qian, X. Zheng, S. Chu, Y. Yang, C. Ding, X. Wang, S. Yu, H. Jiang, Precise fabrication of single-atom alloy co-catalyst with optimal charge state for enhanced photocatalysis, *Natl. Sci. Rev.* 8 (2021) nwaa224–nwaa232, <https://doi.org/10.1093/nsr/nwaa224>.
- [8] K. Lu, Y. Li, F. Zhang, M. Qi, X. Chen, Z. Tang, Y. Yamada, M. Anpo, M. Conte, Y. Xu, Rationally designed transition metal hydroxide nanosheet arrays on graphene for artificial  $\text{CO}_2$  reduction, *Nat. Commun.* 11 (2020) 5181–5189, <https://doi.org/10.1038/s41467-020-18944-1>.
- [9] Z. Jiang, X. Xu, Y. Ma, H. Cho, D. Ding, C. Wang, J. Wu, P. Oleynikov, M. Jia, J. Cheng, Y. Zhou, O. Terasaki, T. Peng, L. Zan, H. Deng, Filling metal-organic framework mesopores with  $\text{TiO}_2$  for  $\text{CO}_2$  photoreduction, *Nature* 586 (2020) 549–554, <https://doi.org/10.1038/s41586-020-2738-2>.
- [10] G. Wang, C. He, R. Huang, J. Mao, D. Wang, Y. Li, Photoinduction of Cu single atoms decorated on  $\text{UiO}-66-\text{NH}_2$  for enhanced photocatalytic reduction of  $\text{CO}_2$  to liquid fuels, *J. Am. Chem. Soc.* 142 (2020) 19339–19345, <https://doi.org/10.1021/jacs.0c09599>.
- [11] F. Xu, K. Meng, B. Cheng, S. Wang, J. Xu, J. Yu, Unique S-scheme heterojunctions in self-assembled  $\text{TiO}_2/\text{CsPbBr}_3$  hybrids for  $\text{CO}_2$  photoreduction, *Nat. Commun.* 11 (2020) 4613–4621, <https://doi.org/10.1038/s41467-020-18350-7>.
- [12] X. Deng, R. Liu, S. Wu, L. Wang, J. Hu, J. Ma, W. Jiang, N. Zhang, X. Zheng, C. Gao, L. Wang, Q. Zhang, J. Zhu, Y. Xiong, Metal-organic framework coating enhances the performance of  $\text{Cu}_2\text{O}$  in photoelectrochemical  $\text{CO}_2$  reduction, *J. Am. Chem. Soc.* 141 (2019) 10924–10929, <https://doi.org/10.1021/jacs.9b06239>.

[13] A. Zhou, Y. Dou, C. Zhao, J. Zhou, X. Wu, J. Li, A leaf-branch  $\text{TiO}_2$ /carbon@MOF composite for selective  $\text{CO}_2$  photoreduction, *Appl. Catal. B-Environ.* 264 (2020) 118519–118526, <https://doi.org/10.1016/j.apcatb.2019.118519>.

[14] L. Zhang, Y. Guo, C. Guo, T. Chen, C. Feng, S. Qiao, J. Wang, Construction of defective Zeolitic Imidazolate Frameworks with improved photocatalytic performance via Vanillin as modulator, *Chem. Eur. J.* 421 (2021) 127839–127848, <https://doi.org/10.1016/j.cej.2020.127839>.

[15] B. Pattengale, S. Yang, S. Lee, J. Huang, Mechanistic probes of zeolitic imidazolate framework for photocatalytic application, *ACS Catal.* 7 (2017) 8446–8453, <https://doi.org/10.1021/acscatal.7b02467>.

[16] Z. Kong, J. Liao, Y. Dong, Y. Xu, H. Chen, D. Kuang, C. Su, Core@Shell  $\text{CsPbBr}_3$ @Zeolitic imidazolate framework nanocomposite for efficient photocatalytic  $\text{CO}_2$  reduction, *ACS Energy Lett.* 3 (2018) 2656–2662, <https://doi.org/10.1021/acsenergylett.8b01658>.

[17] S. Wang, Y. Wang, S. Zang, X. Lou, Hierarchical hollow heterostructures for photocatalytic  $\text{CO}_2$  reduction and water splitting, *Small Methods* 4 (2020) 1900586–1900596, <https://doi.org/10.1002/smtd.201900586>.

[18] G. Ren, S. Liu, Z. Li, H. Bai, X. Hu, X. Meng, Highly selective photocatalytic reduction of  $\text{CO}_2$  to  $\text{CO}$  over Ru-modified  $\text{Bi}_2\text{MoO}_6$ , *Sol. RRL* 6 (2022) 2200154–2200160, <https://doi.org/10.1002/solr.202200154>.

[19] S. Wang, L. She, Q. Zheng, Y. Song, Y. Yang, L. Chen, Ag-doped  $\text{CuV}_2\text{O}_6$  nanowires for enhanced visible-light photocatalytic  $\text{CO}_2$  reduction, *Ind. Eng. Chem. Res.* 62 (2023) 455–465, <https://doi.org/10.1021/acs.iecr.2c03655>.

[20] Y. Ma, X. Yi, S. Wang, T. Li, B. Tan, C. Chen, T. Majima, E. Wacławik, H. Zhu, J. Wang, Selective photocatalytic  $\text{CO}_2$  reduction in aerobic environment by microporous Pd-porphyrin-based polymers coated hollow  $\text{TiO}_2$ , *Nat. Commun.* 13 (2022) 1400–1409, <https://doi.org/10.1038/s41467-022-29102-0>.

[21] Y. Zhu, C. Gao, S. Bai, S. Chen, R. Long, L. Song, Z. Li, Y. Xiong, Hydriding Pd cocatalysts: an approach to giant enhancement on photocatalytic  $\text{CO}_2$  reduction into  $\text{CH}_4$ , *Nano Res.* 10 (2017) 3396–3406, <https://doi.org/10.1007/s12274-017-1552-0>.

[22] Z. Wu, S. Guo, L. Kong, A. Geng, Y. Wang, P. Wang, S. Yao, K. Chen, Z. Zhang, Doping  $[\text{Ru}(\text{bpy})_3]^{2+}$  into metal-organic framework to facilitate the separation and reuse of noble-metal photosensitizer during  $\text{CO}_2$  photoreduction, *Chin. J. Catal.* 42 (2021) 1790–1797, [https://doi.org/10.1016/S1872-2067\(21\)63820-2](https://doi.org/10.1016/S1872-2067(21)63820-2).

[23] Z. Zhao, Z. Liu, A. Zhang, X. Yan, W. Xue, B. Peng, H. Xin, X. Pan, X. Duan, Graphene-nanopocket-encaged PtCo nanocatalysts for highly durable fuel cell operation under demanding ultralow-Pt-loading conditions, *Nat. Nanotechnol.* 17 (2022) 968–975, <https://doi.org/10.1038/s41565-022-01170-9>.

[24] J. Qin, S. Wang, X. Wang, Visible-light reduction  $\text{CO}_2$  with dodecahedral zeolitic imidazolate framework ZIF-67 as an efficient co-catalyst, *Appl. Catal. B-Environ.* 209 (2017) 476–482, <https://doi.org/10.1016/j.apcatb.2017.03.018>.

[25] J. He, W. Chen, H. Gao, Y. Chen, L. Zhou, Y. Zou, R. Chen, L. Tao, X. Lu, S. Wang, Tuning hydrogen binding modes within  $\text{RuO}_2$  lattice by proton and electron codoping for active and stable acidic oxygen evolution, *Chem. Catal. 2* (2022) 578–594, <https://doi.org/10.1016/j.chechat.2022.01.012>.

[26] Y. Miao, H. Zhang, W. Jiang, R. Zhao, Y. Liu, Z. Wang, P. Wang, Z. Zheng, K. Song, W. Wei, Y. Dai, J. He, H. Cheng, B. Huang, An integrated Si photocathode with lithiation-activated molybdenum oxide nanosheets for efficient ammonia synthesis, *Nano Energy* 102 (2022) 107639–107648, <https://doi.org/10.1016/j.nanoen.2022.107639>.

[27] M. Albolkany, Y. Wang, W. Li, S. Arooj, C. Chen, N. Wu, Y. Wang, R. Zboril, R. Fischer, B. Liu, Dual-function HKUST-1: templating and catalyzing formation of graphitic carbon nitride quantum dots under mild conditions, *Angew. Chem. Int. Ed.* 59 (2020) 21499–21504, <https://doi.org/10.1002/anie.202009710>.

[28] Z. Li, X. Zhang, Y. Kang, C. Yu, Y. Wen, M. Hu, D. Meng, W. Song, Y. Yang, Interface engineering of Co-LDH@MOF heterojunction in highly stable and efficient oxygen evolution reaction, *Adv. Sci. 8* (2021) 2002631–2002640, <https://doi.org/10.1002/advs.202002631>.

[29] X. Zhao, H. Yang, P. Jing, W. Shi, G. Yang, P. Cheng, A metal-organic framework approach toward highly nitrogen-doped graphitic carbon as a metal-free photocatalyst for hydrogen evolution, *Small* 13 (2017) 1603279–1603284, <https://doi.org/10.1002/smll.201603279>.

[30] Y. Wang, Y. Du, Z. Fu, J. Ren, Y. Fu, L. Wang, Construction of Ru/FeCoP heterointerface to drive dual active site mechanism for efficient overall water splitting, *J. Mater. Chem. A* 10 (2022) 16071–16079, <https://doi.org/10.1039/D2TA03465D>.

[31] D. Wu, F. He, Y. Dai, Y. Xie, Y. Ling, L. Liu, J. Zhao, H. Ye, Y. Hou, A heterostructured ZnAl-LDH@ZIF-8 hybrid as a bifunctional photocatalyst/adsorbent for  $\text{CO}_2$  reduction under visible light irradiation, *Chem. Eur. J.* 446 (2022) 137003–137012, <https://doi.org/10.1016/j.cej.2022.137003>.

[32] X. Sun, L. Sun, G. Li, Y. Tuo, C. Ye, J. Yang, J. Low, X. Yu, J. Bitter, Y. Lei, D. Wang, Y. Li, Phosphorus tailors the d-band center of copper atomic sites for efficient  $\text{CO}_2$  photoreduction under visible-light irradiation, *Angew. Chem. Int. Ed.* 8 (2022) e202207677–e202207686, <https://doi.org/10.1002/anie.202207677>.

[33] N. Huang, J. Shen, X. Zhang, P. Liao, J. Zhang, X. Chen, Coupling ruthenium bipyridyl and cobalt imidazolate units in a metal-organic framework for an efficient photosynthetic overall reaction in diluted  $\text{CO}_2$ , *J. Am. Chem. Soc.* 144 (2022) 8676–8682, <https://doi.org/10.1021/jacs.2c01640>.

[34] K. Zhu, Q. Zhu, M. Jiang, Y. Zhang, Z. Shao, Z. Geng, X. Wang, H. Zeng, X. Wu, W. Zhang, K. Huang, S. Feng, Modulating  $\text{Ti}^{2+}$  Orbit-occupancy in  $\text{Cu}/\text{TiO}_2$  composite for selective photocatalytic  $\text{CO}_2$  reduction to  $\text{CO}$ , *Angew. Chem. Int. Ed.* (2022) e202207600–e202207609, <https://doi.org/10.1002/anie.202207600>.

[35] M. Xiao, L. Zhang, B. Luo, M. Lyu, Z. Wang, H. Huang, S. Wang, A. Du, L. Wang, Molten-salt-mediated synthesis of an atomic nickel Co-catalyst on  $\text{TiO}_2$  for improved photocatalytic  $\text{H}_2$  evolution, *Angew. Chem. Int. Ed.* 59 (2020) 7230–7234, <https://doi.org/10.1002/anie.202001148>.

[36] N. Meng, C. Liu, Y. Liu, Y. Yu, B. Zhang, Efficient electrosynthesis of syngas with tunable  $\text{CO}/\text{H}_2$  ratios over  $\text{ZnxCd}_{1-x}\text{S}$ -amine inorganic-organic hybrids, *Angew. Chem. Int. Ed.* 58 (2019) 18908–18913, <https://doi.org/10.1002/anie.201913003>.

[37] H. Hong, J. He, Y. Wang, X. Guo, X. Zhao, X. Wang, C. Zhi, H. Li, C. Han, An amino-functionalized metal-organic framework achieving efficient capture-diffusion-conversion of  $\text{CO}_2$  towards ultrafast  $\text{Li}-\text{CO}_2$  batteries, *J. Mater. Chem. A* 10 (2022) 18396–18407, <https://doi.org/10.1039/D2TA05342J>.

[38] K. Guo, X. Li, H. Lei, H. Guo, X. Jin, X. Zhang, W. Zhang, U. Apfel, R. Cao, Role-specialized division of labor in  $\text{CO}_2$  Reduction with doubly-functionalized iron porphyrin atropisomers, *Angew. Chem. Int. Ed.* 61 (2022) e202209602–e202209608, <https://doi.org/10.1002/anie.202209602>.

[39] G. Duan, X. Li, G. Ding, L. Han, B. Xu, S. Zhang, Highly efficient electrocatalytic  $\text{CO}_2$  reduction to  $\text{C}_{2+}$  products on a poly(ionic liquid)-based  $\text{Cu}^{0+}\text{Cu}^{1+}$  tandem catalyst, *Angew. Chem. Int. Ed.* 61 (2022) e202110657–e202110666, <https://doi.org/10.1002/anie.202110657>.